

Variational Image Reconstruction for Dynamic High Resolution Photoacoustic Tomography

Felix Lucka¹, Marta Betcke¹, Nam Huynh², Edward Zhang², Paul Beard², Ben Cox² and Simon Arridge¹

1) Department of Computer Science 2) Department of Medical Physics
University College London, WC1E 6BT London, UK

contact: f.lucka@ucl.ac.uk



Compressed Photoacoustic Sensing

Current PAT systems offer either exquisite image quality or high frame rates but not both. As the spatio-temporal complexity of many absorbing tissue structures is rather low, the data recorded is often highly redundant. Therefore, developing systems that only sense the non-redundant part of the data can increase the acquisition speed. We examine the acceleration of sequential Fabry-Pérot scanners (**Fig 1**) by random single-point (rSP) or patterned interrogation (sHd) sub-sampling (**Fig 2**).

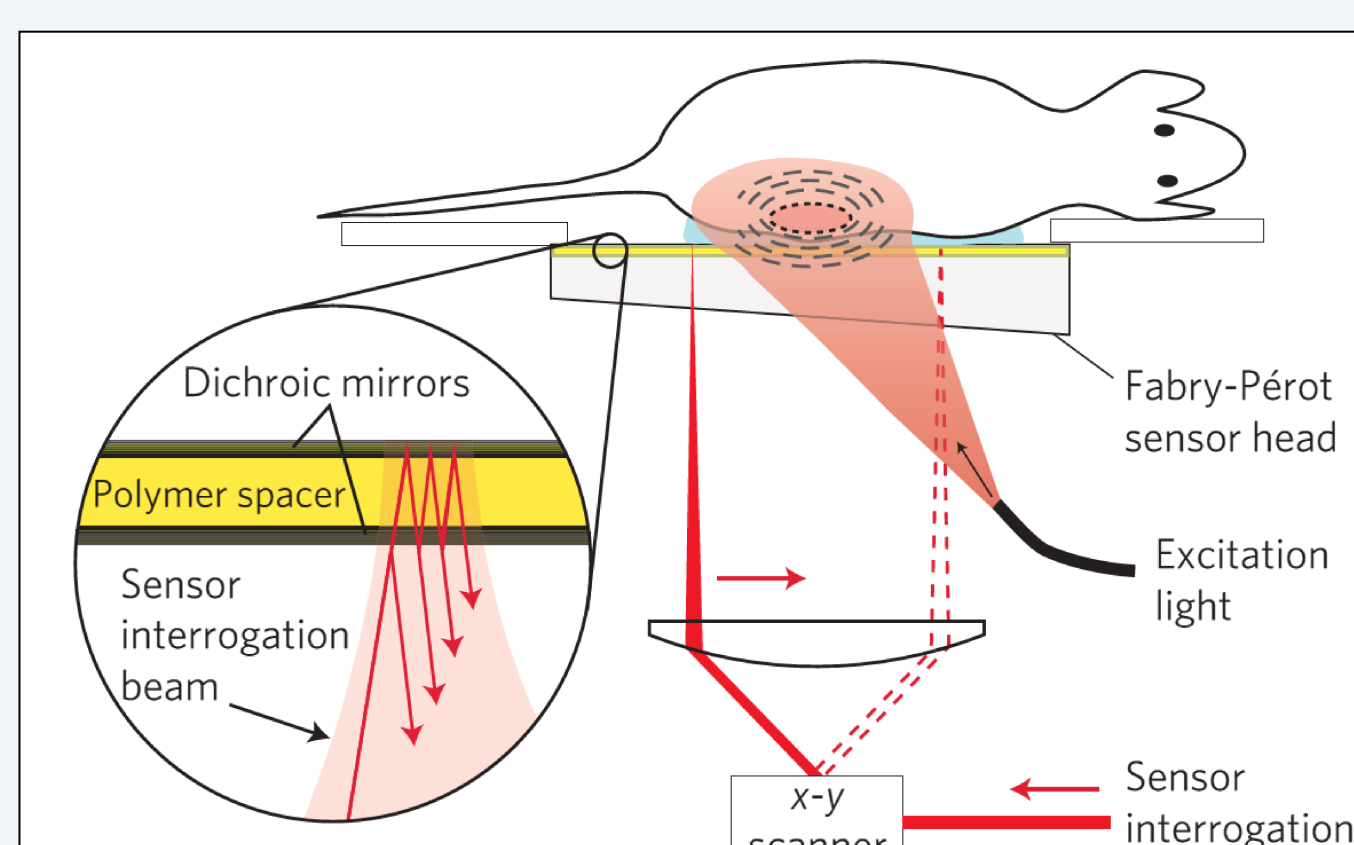


Fig. 1: Standard Fabry-Pérot (FB) scanners raster-sample the incident photoacoustic field sequentially with a high spatial resolution and sensitivity at the expense of a long acquisition time (cf. Zhang et al., 2008).

Sparse Variational Image Reconstruction

We need to solve $f = GAp_0$, with G sub-sampling and A forward operator. As conventional approaches fail when used on sub-sampled data (cf. **Fig 4**), we employ sparse variational regularization (e.g., *total variation*, TV),

$$\hat{p}_\lambda = \operatorname{argmin}_{p \geq 0} \frac{1}{2} \|f - GAp\|_2^2 + \lambda \mathcal{J}(p) \quad (1)$$

enhanced by *Bregman iterations* (Osher et al, 2005),

$$\hat{p}_\lambda^{k+1} = \operatorname{argmin}_{p \geq 0} \frac{1}{2} \|(f + b^k) - GAp\|_2^2 + \lambda \mathcal{J}(p)$$

$$b^{k+1} = b^k + f - GAp^{k+1}; \quad b_1 = 0$$

to compensate for the systematic bias of (1) (cf. **Fig 5**).

Solving (1) by first order optimization schemes (Burger et al., 2014), requires to evaluate A and A^* . Our implementation relies on a *k*-space *pseudo-spectral method* for 3D acoustic wave propagation (Treeby & Cox, 2010) which utilizes GPU computing to cope with the immense computational challenges. We derived and examined an analytical representation of A^* in Arridge et al., 2016b.

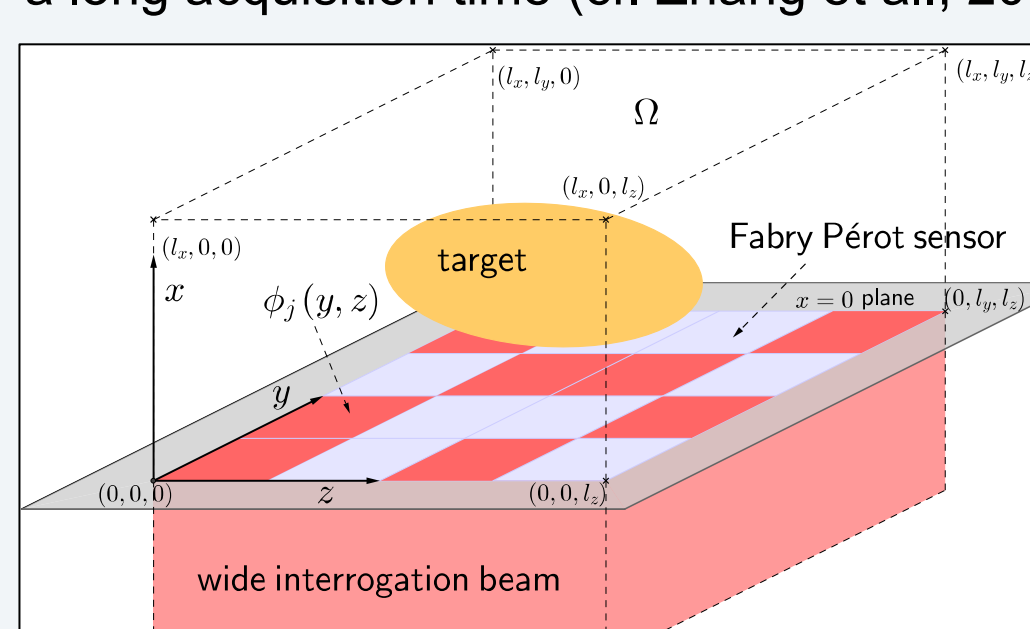


Fig. 2 (left): Patterned interrogation (principle): The FP sensor is interrogated by a light pattern (Huynh et al., 2014).

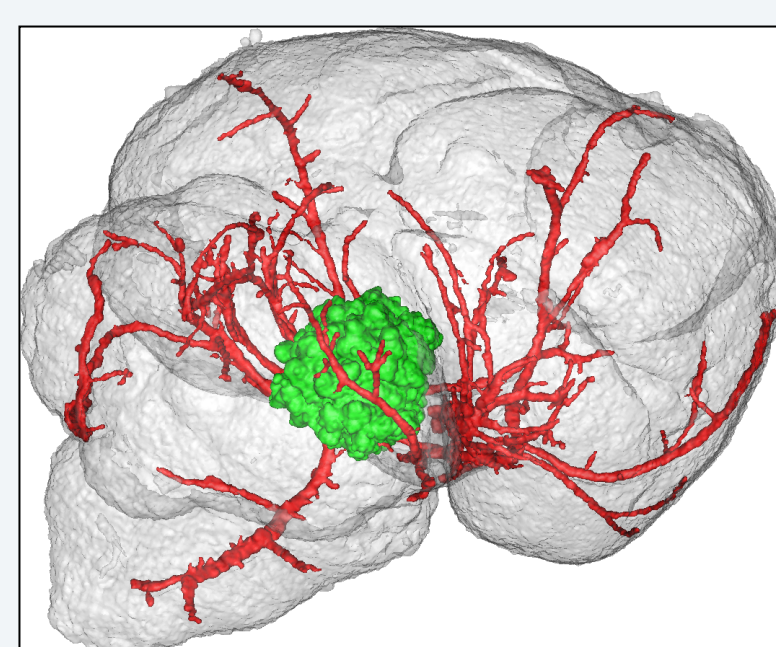


Fig. 3 (left): Numerical phantom derived from a micro-CT scan of a mouse brain for simulating the perfusion of vascular (red) and tumorous (green) brain tissue.

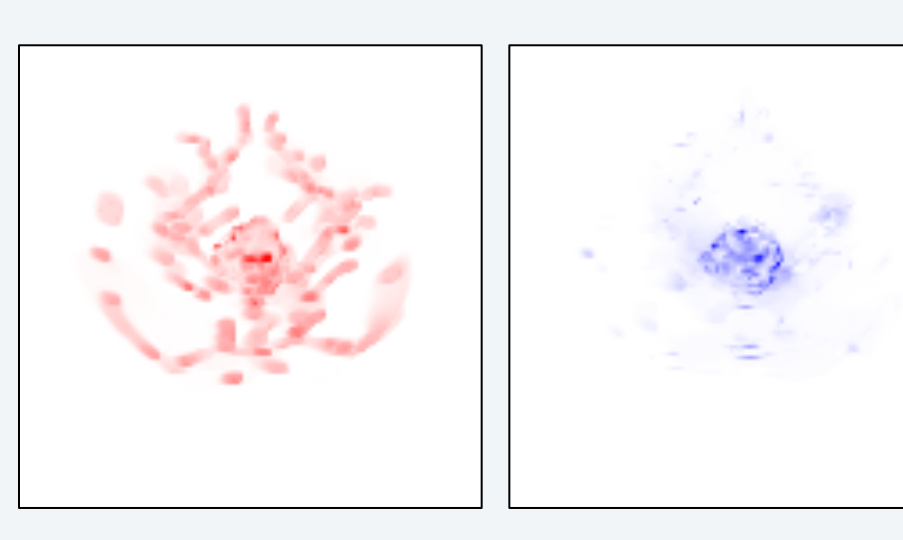


Fig. 5: Difference between normal TV regularized solution and Bregman iterations. Left: Positive part of the difference in red colour scale. Right: Negative part of the difference in blue colour scale.

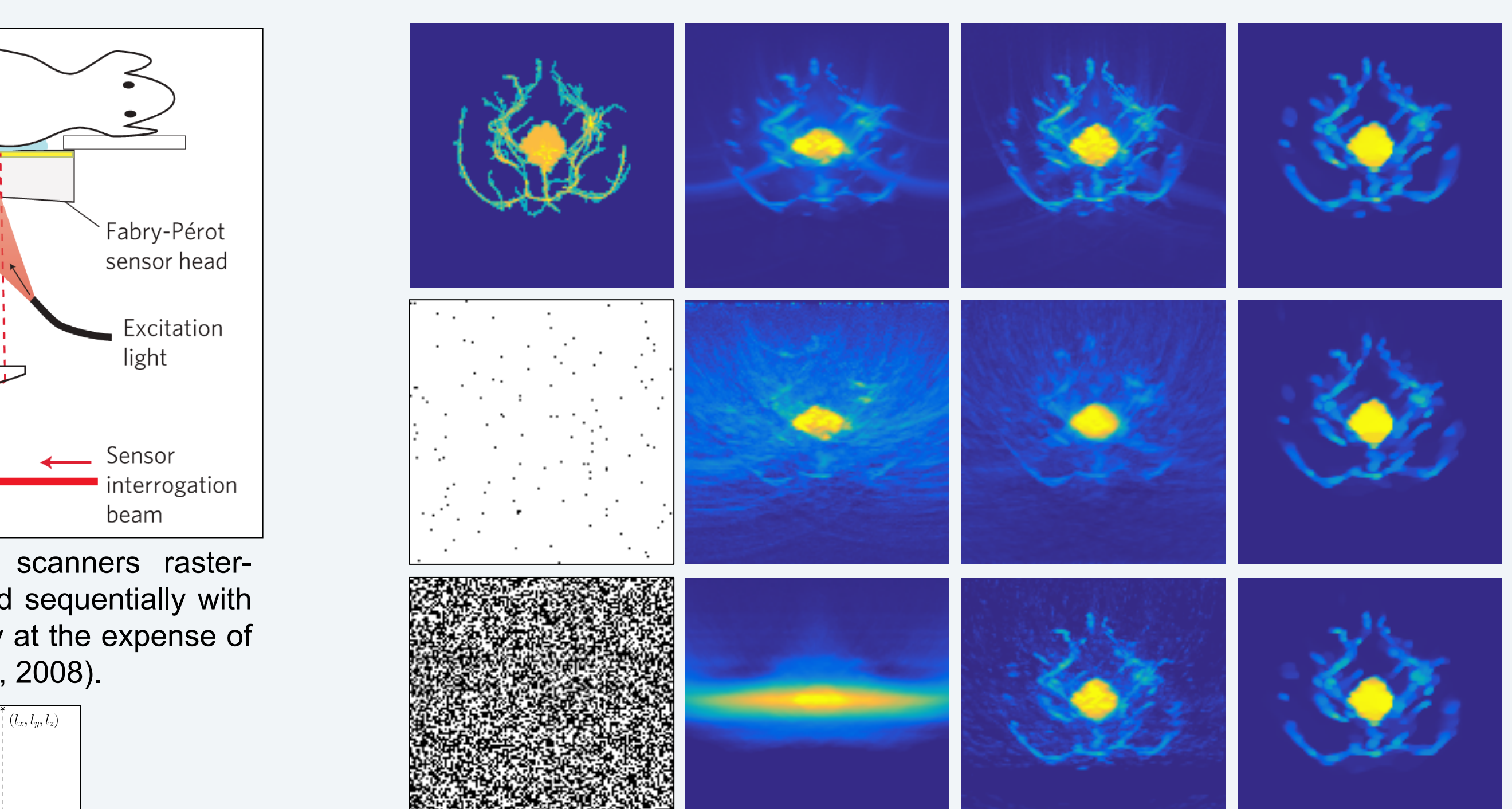


Fig. 4 (above): "Best-case"-study: Phantom (Fig 3) is close to the detection plane (top edge), has high contrast, all acoustic parameters are assumed known and the acoustic field is sampled at Nyquist frequency in space and time. Col 1: Maximum intensity projection (mxIP) of phantom and sketches of rSP and sHd sub-sampling (acceleration factor 128 = 0.78% of the original data). Col 2-4: mxIPs of time reversal (TR, cf. Treeby & Cox, 2010), L2 regularization and TV regularization with Bregman iterations for conventionally scanned, rSP and sHd data (row 1-3).

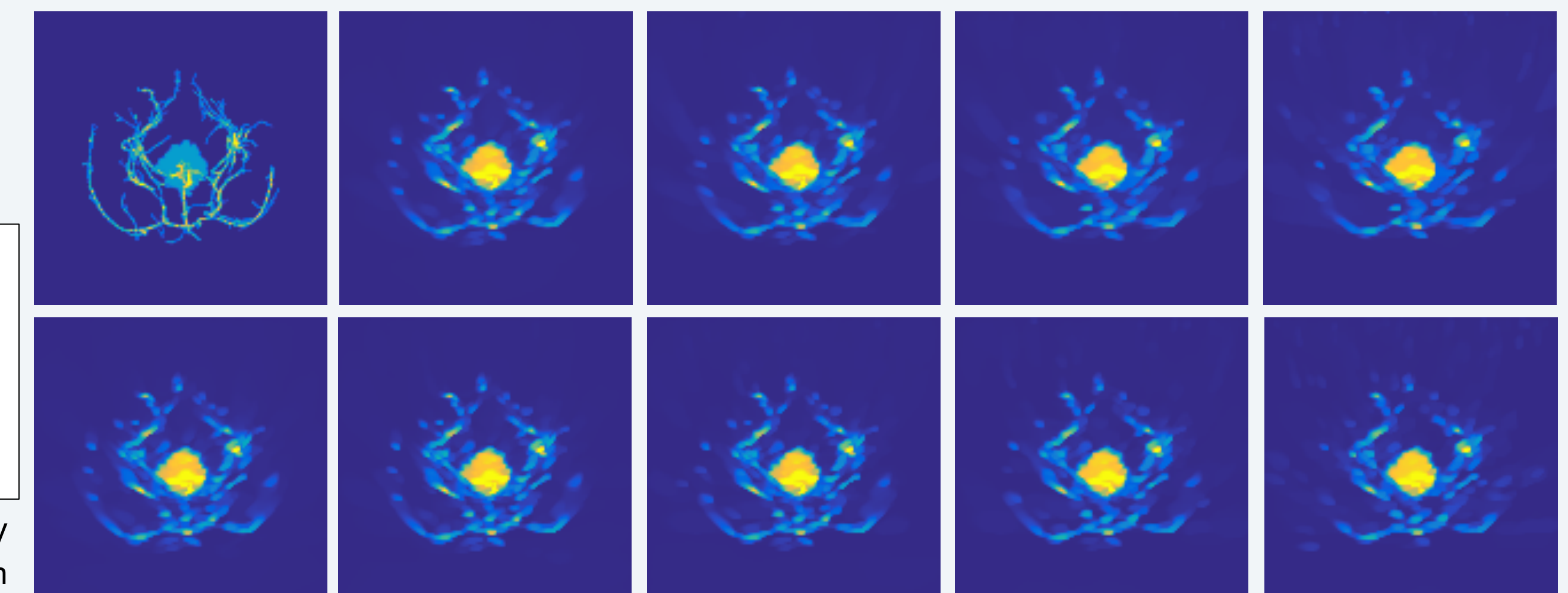


Fig. 6: "Realistic-case"-study: The phantom is more distant to the detection plane (top edge), has a lower contrast, the forward model is inaccurate and even for the "full" data, the acoustic field is spatially undersampled. Col 1: mxIP of phantom and Bregman iteration for "full" data (i.e., regularly sub-sampled by a factor of 4). Col 2-5: mxIPs of Bregman iterations for rSP (row 1) and sHd (row 2) sub-sampling with factors 1,4,8,16 (col 2,3,4,5).

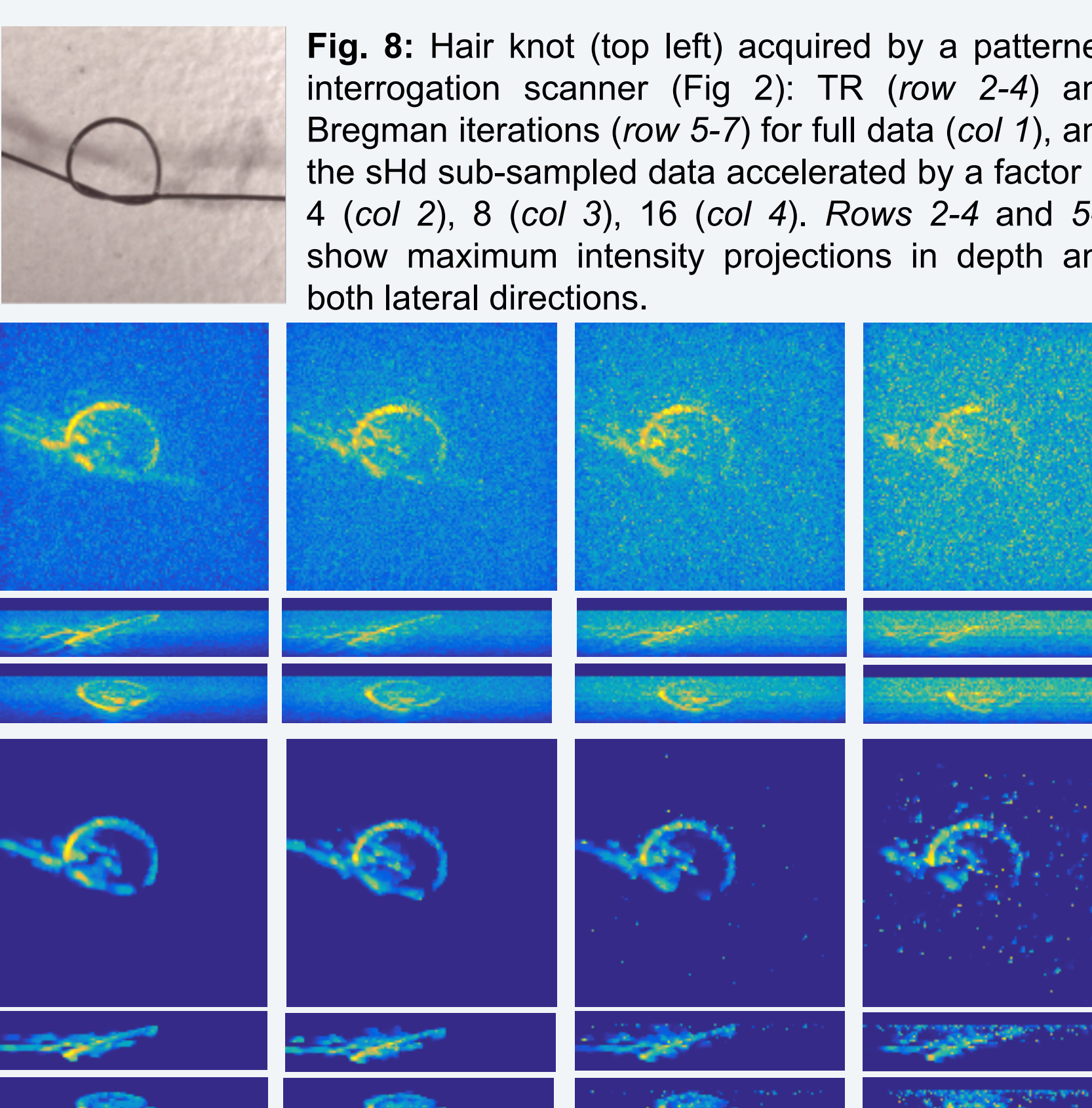


Fig. 8: Hair knot (top left) acquired by a patterned interrogation scanner (Fig 2): TR (row 2-4) and Bregman iterations (row 5-7) for full data (col 1), and the sHd sub-sampled data accelerated by a factor of 4 (col 2), 8 (col 3), 16 (col 4). Rows 2-4 and 5-7 show maximum intensity projections in depth and both lateral directions.

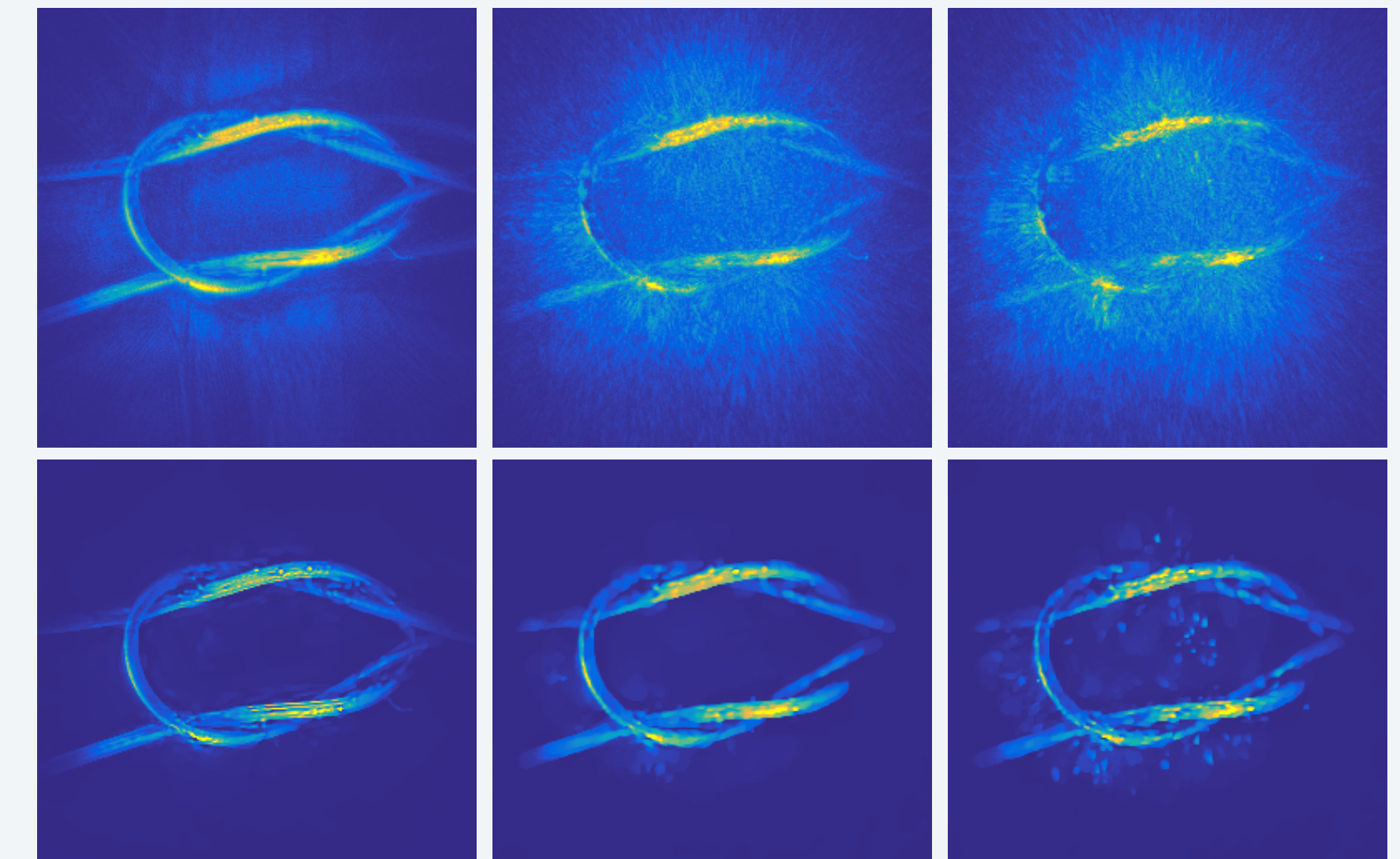


Fig. 7: Reconstructions of one frame of a dynamic experimental phantom: TR (row 1) and Bregman iterations (row 2) for full data (col 1) rSP sub-sampling by a factor of 4 (col 2) and 8 (col 3).

Results and Discussion

We first evaluated our methods with simulated data from a realistic phantom (**Fig 3**): In general, using sparse variational methods is essential to obtain high quality reconstructions from sub-sampled data (**Fig 4**). The comparison between "best-case" (**Fig 4**) and "realistic-case" data (**Fig 6**) reveals that the acceleration factor achievable heavily depends on the quality of the data. Furthermore, sHd slightly outperforms rSP sub-sampling. **Fig 7,8,9** show the results for experimental data: The acceleration factors achievable are similar to the "realistic-case" simulation study: Various non-trivial difficulties such as developing pre-processing routines and more accurate forward models will have to be overcome to realize higher acceleration factors (> 8). **Fig 9** also reveals that the TV regularization used here is not suitable to recover thin, vessel-like structures but tends to break them apart.

Conclusion and Outlook

PAT wave fields can be highly compressible but a substantial acceleration of current sequential PAT scanners requires:

- Variational image reconstruction employing spatial sparsity constraints matching the structure of the target. Typical PAT targets, such as vasculature-rich images, need more sophisticated regularization terms than TV.
- An accurate forward model well-aligned with the data. This requires refined data pre-processing, and data-driven model calibration.

The full results can be found in Arridge et al., 2016a. Further acceleration of dynamic PAT requires variational methods employing spatio-temporal sparsity constraints which also exploit the temporal redundancy of data generated by dynamics of low complexity.

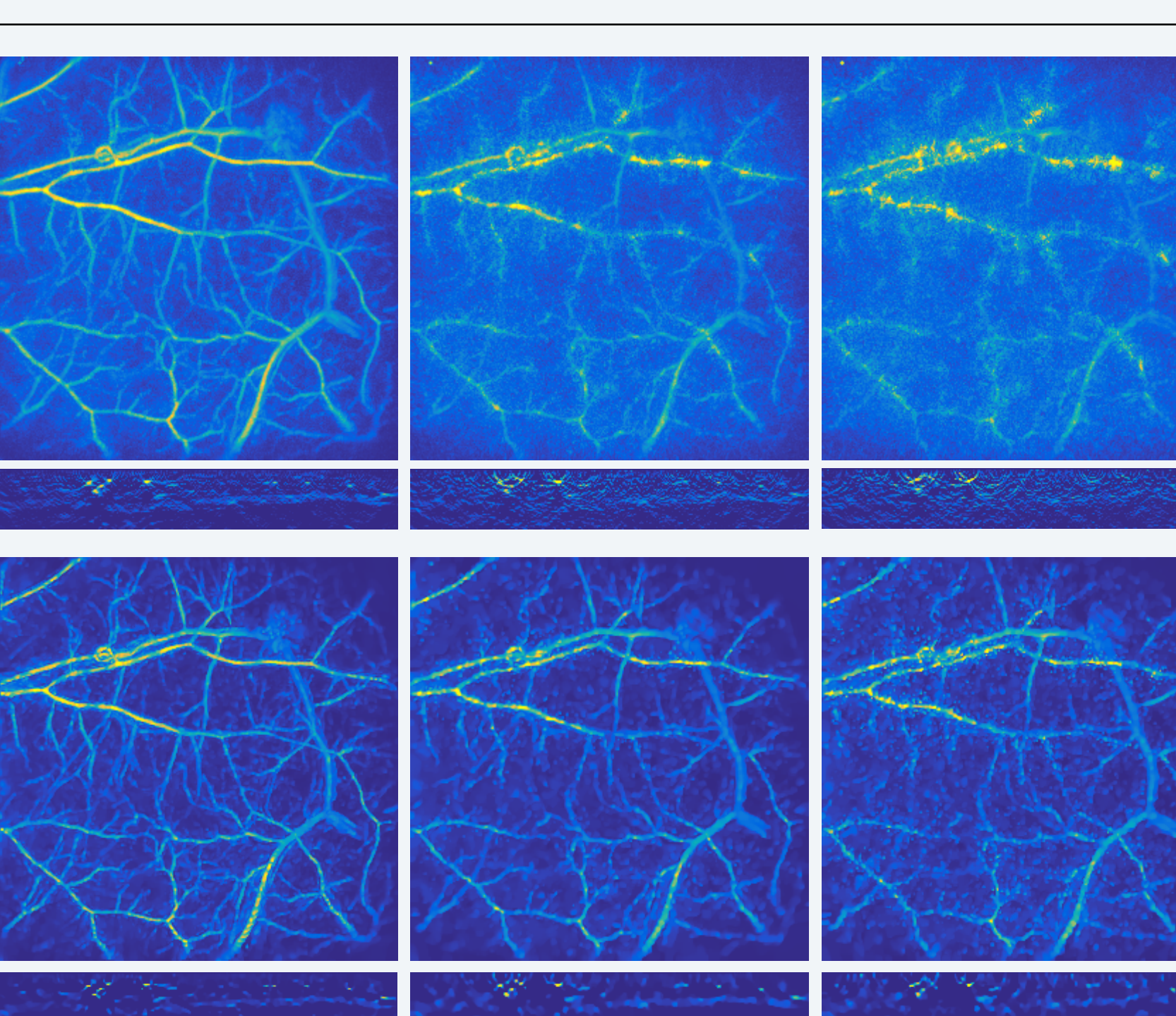


Fig. 9: In-vivo data of the skin vasculature of a mouse acquired by a standard FP scanner: Comparison between TR (row 1-2) and TVBreg (row 3-4) for full data (col 1), rSP sub-sampling by factor 4 (col 2) and 8 (col 3). Rows 1+3 show depth-mxIP, rows 2+4 a vertical slice.

- ## References & Acknowledgements
- Arridge, Beard, Betcke, Cox, Huynh, Lucka, Ogunlade, Zhang, 2016. Accelerated High-Resolution Photoacoustic Tomography via Compressed Sensing. *Physics in Medicine & Biology* (accepted).
 - Arridge, Betcke, Cox, Lucka, Treeby, 2016. On the Adjoint Operator in Photoacoustic Tomography. *Inverse Problems* 32(11).
 - Burger, Sawatzky, Steidl, 2014. First Order Algorithms in Variational Image Processing, *arXiv:1412.4237*.
 - Huynh, Zhang, Betcke, Arridge, Beard, Cox, 2014. Patterned interrogation scheme for compressed sensing photoacoustic imaging using a Fabry Perot planar sensor, *Proc. SPIE*, 8943.
 - Osher, Burger, Goldfarb, Xu, Yin, 2006. An iterative regularization method for total variation-based image restoration, *Multiscale Modeling and Simulation*, 2(4).
 - Zhang, Laufer, Beard, 2008. Backward-mode multi-wavelength photoacoustic scanner using a planar fabry-perot polymer film ultrasound sensor for high-resolution three-dimensional imaging of biological tissues, *Applied Optics*, 47(4).
 - Treeby, Cox, 2010. k-Wave: MATLAB toolbox for the simulation and reconstruction of photoacoustic wave fields, *Journal of Biomedical Optics*, 2(15).

We gratefully acknowledge the support of NVIDIA Corporation with the donation of the Tesla K40 GPU used for this research.

